

Suppressing Charge Disproportionation of MnO₂ Cathodes in Rechargeable Zinc Ion Batteries via Cooperative Jahn-Teller Distortion

Jiyun Heo⁺^[a] Sanggyu Chong⁺^[a] Soohyun Kim,^[a] Riyul Kim,^[a] Kyungjae Shin,^[a] Jihan Kim,^{*[a, b]} and Hee-Tak Kim^{*[a, b]}

MnO₂ is a promising candidate material as intercalative cathodes in rechargeable aqueous zinc ion batteries (ZIBs). It is renowned for its low cost, minimal toxicity, and high energy density; however, severe capacity fading from the dissolution of MnO₂ remains a critical challenge that must be overcome to achieve improved cycling performance. In this study, surface coating of MnO₂ with dicyandiamide is proposed as a method to significantly reduce the dissolution of MnO₂ by addressing the fundamental cause of MnO₂ dissolution, which is the charge disproportionation (CD) reaction of Mn³⁺. Experimental and

computational methods are used to demonstrate that the surface coating triggers cooperative Jahn-Teller distortion of Mn⁴⁺ to alleviate lattice distortion and impede the CD reaction. Thus, the cycling stability of MnO₂ is significantly improved, exhibiting 170% higher capacity in comparison with pristine MnO₂ and 99.9% coulombic efficiency under a 1C rate condition. Resolving the orbital degeneracy with surface modification will open a new and prospective path for superior cycling performance of MnO₂-based ZIBs.

1. Introduction

Secondary batteries using aqueous electrolytes have garnered a great amount of interest in both research institutes and commercial markets due to their non-flammability and potentially lower cost in comparison to organic electrolyte-based Li batteries, which are currently the battery of choice for large scale-energy storage systems (ESSs).^[1–4] Among various aqueous batteries, metallic zinc batteries have emerged in the recent years due to their multiple attractive properties (e.g. low Zn/Zn²⁺ redox potential (-0.76 V versus standard hydrogen electrode), high gravimetric and volumetric capacity (820 mAh g⁻¹ and 5855 mAh cm⁻³, respectively), and safety, as well as the low cost of zinc metal).^[5,6] In particular, rechargeable mild acid Zn-ion batteries (ZIBs) that use the intercalation chemistry of Zn ions promise to be a new electrochemical energy storage technology because the appropriate pH conditions can help avoid unwanted H₂O reactions.^[7]

In the past, various materials have been considered to be used as cathodes in ZIB,^[8–12] and amongst them, manganese

oxide (typically MnO₂) is typically acknowledged as one of the most promising materials due to its high working voltage and appreciable specific capacity. Among several MnO₂ polymorphs, layered-type δ -MnO₂ with large interlayer spacing is prominently considered for ZIB systems because of its larger Zn ion storage capacity compared to other polymorphs (α -, β -, γ -, and λ -type MnO₂).^[13] However, δ -MnO₂ cathodes exhibit two fundamental challenges that must be overcome before their successful incorporation onto ZIB: 1) poor electron conductivity and 2) dissolution of Mn²⁺. Including modification of MnO₂ with highly conductive materials such as carbon,^[14–16] several strategies to enhance the electron conductivity of MnO₂ have been proposed, but the Mn²⁺ dissolution issue remains a critical obstacle.

The problematic Mn²⁺ dissolution of MnO₂ originates from the lability of Mn³⁺. Electrically degenerate Mn³⁺ has high and unstable energy states; therefore, partakes in a relaxation process called charge disproportionation (CD) reaction. In this reaction, two Mn³⁺ species are combined to produce electrically non-degenerate Mn²⁺ and Mn⁴⁺, which in turn reduces the total energy of MnO₂. However, as Mn²⁺ is highly soluble in the electrolyte, CD reaction subsequently leads to Mn²⁺ dissolution from MnO₂. Therefore, Mn²⁺ additives, such as MnSO₄, are conventionally added to the electrolyte coupled with MnO₂ cathode to mitigate dissolution.^[17] Nevertheless, continued reports of low capacity retention even with the Mn²⁺-containing electrolytes suggest that MnO₂ dissolution is not fully prevented by the additives.^[18] Several works have also demonstrated notable improvements in capacity retention by physically preventing Mn²⁺ dissolution via coating the surface of MnO₂ with amorphous layers,^[19–21] or by using inner fillers.^[22,23] However, these approaches can only physically suppress dissolution and fail to target the fundamental cause

[a] J. Heo,⁺ S. Chong,⁺ Dr. S. Kim, Dr. R. Kim, K. Shin, Prof. J. Kim, Prof. H.-T. Kim

Department of Chemical and Biomolecular Engineering
Korea Advanced Institute of Science and Technology
291 Daehak-ro, Yuseong-gu, Daejeon 34141, Republic of Korea

[b] Prof. J. Kim, Prof. H.-T. Kim
Advanced Battery Center, KAIST Institute for the NanoCentury
Korea Advanced Institute of Science and Technology
335 Gwahangno, Yuseong-gu, Daejeon 34141, Republic of Korea
E-mail: jihankim@kaist.ac.kr
heetak.kim@kaist.ac.kr

[+] These authors contributed equally to this work.

Supporting information for this article is available on the WWW under
<https://doi.org/10.1002/batt.202100181>

of the formation of the Mn^{2+} . Therefore, new strategy development that can specifically target the origin of the CD reaction is imperative.

Jahn-Teller distortion (JTD), which leads to the elimination of orbital degeneracy, can be viewed as an alternative pathway for material relaxation. JTD often occurs in transition metals with degenerate electronic structures, and Mn^{3+} is one such JT-active center. When $[MnO_6]^{3+}$ undergoes JTD, the octahedral geometry of the metal complex is elongated along a single axis, breaking the orbital degeneracy. JTD of Mn^{3+} has been previously observed in Li-based batteries that uses manganese oxides as a cathode material, which suggests that JTD is possible even in crystalline structures.^[24] However, Mn^{3+} in MnO_2 is often hindered from fully partaking in JTD by the presence of neighboring Mn^{4+} species, which prevents the geometrical elongation required for JTD. As a result, the JTD around Mn^{3+} exhibits pseudo-degeneracy rather than a fully resolved degeneracy state; hence, CD reaction cannot be sufficiently prevented.^[25,26] Furthermore, the JTD around Mn^{3+} causes unfavorable buckling of the MnO_2 lattice, which stems from the geometrical differences between Mn^{3+} and Mn^{4+} complexes.^[27] Such effects altogether lead to the instability of Mn^{3+} in MnO_2 and force Mn^{3+} to participate in CD. Therefore, a novel method is needed that can allow Mn^{3+} to easily undergo JTD even in the presence of neighboring Mn^{4+} while concurrently suppressing the undesirable buckling effect.

In this paper, we propose that coating the surface of MnO_2 with dicyandiamide (DCDA) can suppress the unwanted Mn dissolution by inducing cooperative Jahn-Teller distortion (CJTD) of Mn^{4+} (Figure 1). CJTD refers to a phenomenon in which the distortion of molecular orbitals is observed even at the JT-inactive centers due to the influence of neighboring JT-active sites or other external factors. The selection of DCDA is based on its capability to anchor onto the metal oxide with its amine functional groups, and on the strong π donor (DCDA) - acceptor (MnO_2) interaction, which can then trigger the CJTD of Mn^{4+} complexes.^[28-31] We found that the decoration of the MnO_2 surface with DCDA induces CJTD of JT-inactive Mn^{4+} -centered $[MnO_6]$ and improves the lattice uniformity and

stabilizes the MnO_2 slabs by reducing the steric stress. As a result, the DCDA coating reduces the dissolution of Mn^{2+} and notably improves the cycling stability. Based on spectroscopic and DFT analyses, we present the possibility of CJTD around Mn^{4+} and of CJTD-assisted JTD around Mn^{3+} while preventing the buckling phenomenon. We believe our findings can provide new insights that address the Mn dissolution issue toward improved MnO_2 stability for ZIB.

2. Results and Discussion

2.1. Characterization of DCDA-Coated δ - MnO_2

Among the amine containing species, dicyandiamide (DCDA) was specifically chosen for coating material because it has the lowest electron density around the proton within the amine group, which can facilitate strong anchoring on MnO_2 surface (Figure S1). DCDA-coated MnO_2 samples are denoted as x-d- MnO_2 , where x stands for the wt% ratio of DCDA and MnO_2 . Because δ - MnO_2 is known to be quite labile as a result of its low coordinated oxygen species on the surface, it can be reduced during the surface treatment. To check the chemical stability during the surface coating, 20-d- MnO_2 was examined by scanning electron microscopy (SEM), scanning transmission electron microscopy (STEM), and X-ray photoelectron spectroscopy (XPS), and the results were compared with those obtained for pristine MnO_2 (p- MnO_2). According to their SEM images [Figure 2(a)], p- MnO_2 and 20-d- MnO_2 do not differ in morphology, indicating that DCDA is homogeneously distributed on the surface of MnO_2 without forming bulk DCDA aggregates. The uniform distribution of DCDA over MnO_2 surfaces is further confirmed by the evenly-distributed N signals in the STEM energy dispersive X-ray spectroscopy (STEM-EDX) mapping image [Figure 2(a)].

The high-resolution Mn 2p XPS spectra for p- MnO_2 and 20-d- MnO_2 are shown in Figure 2(b and c), respectively. The two characteristic peaks can be deconvoluted into Mn^{3+} (642 and 653 eV) and Mn^{4+} (643 eV and 654 eV) peaks.^[13,32] The Mn^{3+} / Mn^{4+} ratios determined from the XPS spectra were 0.394 for p- MnO_2 and 0.395 for 20-d- MnO_2 (Table S1). Their similar values indicate the absence of chemical reaction between MnO_2 and DCDA and the preservation of the compositional feature of pristine MnO_2 with the DCDA coating. However, the maximum peak at around 642 eV shifted to a lower binding energy (641.98 to 641.73 eV) with the DCDA coating (Table S1), indicating an increase in electron density around Mn species due to the π donor-acceptor interaction. The presence of the peaks from amine, cyanide, and C-NC bond in the N 1s spectrum of 20-d- MnO_2 [Figure 2(d)] again confirms the successful incorporation of DCDA on the surface of MnO_2 .

To consolidate the preservation of the δ - MnO_2 structure after the DCDA coating, X-ray powder diffraction (XRD) analysis was further conducted. As shown in Figure 2(e), the peaks from the layered MnO_2 (δ - MnO_2 , JCPDS No. 00-042-1317) were found for both p- MnO_2 and 20-d- MnO_2 . The peak positions, which can trace a structural change by CJTD, will be analyzed later.



Figure 1. Schematic illustration of the proposed strategy. While pristine MnO_2 suffers from distorted lattice with severe dissolution of Mn^{2+} due to the structure differences between Mn^{3+} and Mn^{4+} , DCDA-coated MnO_2 shows highly uniform surface without loss of host material via CJTD of Mn^{4+} .

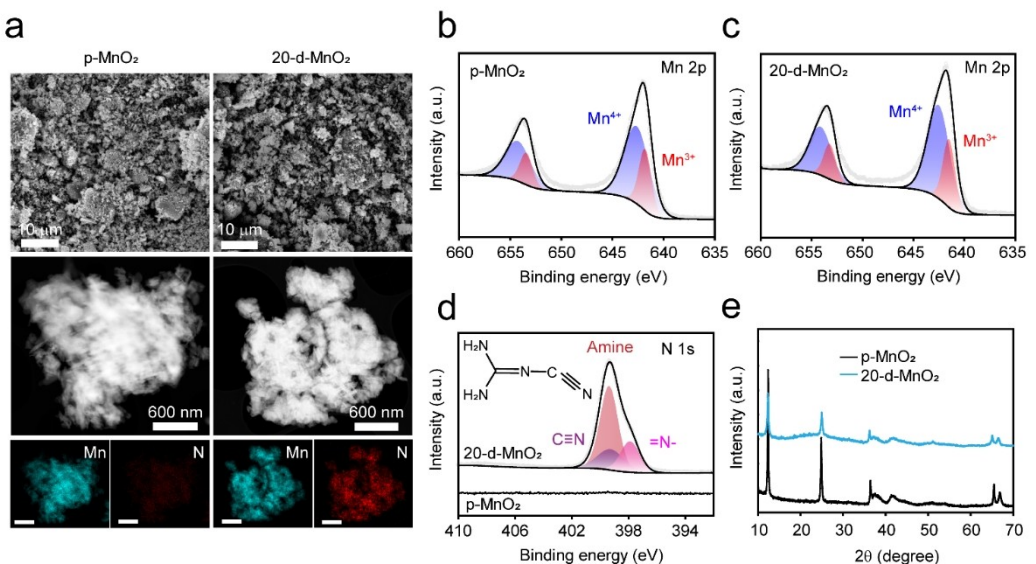


Figure 2. Physical and chemical characterization of DCDA-coated MnO_2 . a) SEM and STEM images with Mn and N elemental mapping of p- MnO_2 (left) and 20-d- MnO_2 (right) particles. Mn 2p XPS spectra of b) p- MnO_2 and c) 20-d- MnO_2 . d) N 1s XPS spectra and e) XRD patterns of p- MnO_2 (bottom) and 20-d- MnO_2 (top).

Besides the peaks from the $\delta\text{-MnO}_2$ structure, 20-d- MnO_2 exhibited a broad band from the amorphous DCDA layer at around $20^\circ\text{--}25^\circ$. When the DCDA content was higher than 20 wt%, the XRD patterns from bulk DCDA crystallite appeared (Figure S2). To avoid any influences from bulk DCDA crystallites, DCDA content was limited up to 20 wt%.

2.2. Suppressing the Mn Dissolution by Surface Coating with DCDA

To assess the effect of DCDA coating, electrochemical tests were conducted with p-, 5-d-, 10-d-, and 20-d- MnO_2 as cathode active materials. Figure 3(a) shows the cycling performance of the cathodes at a low C-rate of C/3 ($1\text{C}=308 \text{ mA g}^{-1}$). MnO_2 -based ZIBs are known to show an increased capacity at early cycles as MnO_2 undergoes an activation process and, subsequently, a decreased capacity due to Mn dissolution and irreversible Zn^{2+} intercalation.^[33] The p- MnO_2 and d- MnO_2 tested in this work showed typical cycling behaviors. However, their discharge capacities differed according to the DCDA content. The discharge capacities of the p- MnO_2 and 5-d- MnO_2 electrodes were indifferent, whereas, for the electrodes with a higher DCDA content, the discharge capacities were augmented with increased DCDA content. The discharge capacities at the 50th cycle were 160, 200, and 220 mA h g^{-1} for p- MnO_2 , 10-d- MnO_2 and 20-d- MnO_2 , respectively. The capacity retention at the 50th cycle with respect to the maximum discharge capacity was higher by more than 30% for 20-d- MnO_2 than that for p- MnO_2 .

For p- MnO_2 and 20-d- MnO_2 , the galvanostatic charge/discharge curves at selected cycles are provided in Figure 3(b). Although further investigation would be needed to fully reveal the redox mechanism of MnO_2 cathode as there are various

proposed charge storage mechanisms,^[34,35] most studies have suggested co-intercalation of Zn^{2+} and H^+ as the most convincing mechanism to date.^[36–39] Based on this mechanism, the clearly distinguished higher and lower discharge plateaus correspond to H^+ and Zn^{2+} intercalation, respectively. The lower voltage plateau was gradually shortened with cycling for both the cathodes due to the irreversible Zn^{2+} intercalation/deintercalation process of MnO_2 . However, the stability of the higher voltage plateau was quite different between p- MnO_2 and 20-d- MnO_2 . The p- MnO_2 cathode suffered from concurrent diminution of the higher and lower voltage plateaus with cycling, while the 20-d- MnO_2 cathode exhibited a high stability of the higher voltage plateau. Because H^+ intercalation/deintercalation is a highly reversible process, the degradation of the higher voltage plateau can be regarded as a consequence of MnO_2 dissolution; thus, the stability of the higher voltage plateau for 20-d- MnO_2 suggests suppression of MnO_2 dissolution.

As direct evidence of the suppressed MnO_2 dissolution for 20-d- MnO_2 , we measured the amounts of Mn and Zn ions in the electrolytes after the cycling test by ICP analysis. As shown in Figure 3(c), the Mn/Zn atomic ratio for 20-d- MnO_2 was 35% lower than that for p- MnO_2 after the cell test, which suggest suppression of Mn dissolution for 20-d- MnO_2 . Considering that the Mn dissolution stems from the CD of vulnerable Mn^{3+} , it accompanies a decreased Mn^{3+} content in the MnO_2 cathode. From the Mn 2p XPS spectra of p- MnO_2 and 20-d- MnO_2 after cycling [Figure 3(d)], the area ratios of Mn^{3+} (641 eV) and Mn^{4+} (642 eV) were quantified. The ratio was about 1.5 times larger for 20-d- MnO_2 (42.4%) than that for p- MnO_2 (25.8%), indicating a diminished CD reaction with the DCDA coating.

Mn dissolution concomitantly leads to a defect in the MnO_2 , forming an Mn–OH bond. The O 1s spectra of the p- MnO_2 and 20-d- MnO_2 electrode display two representative peaks attrib-

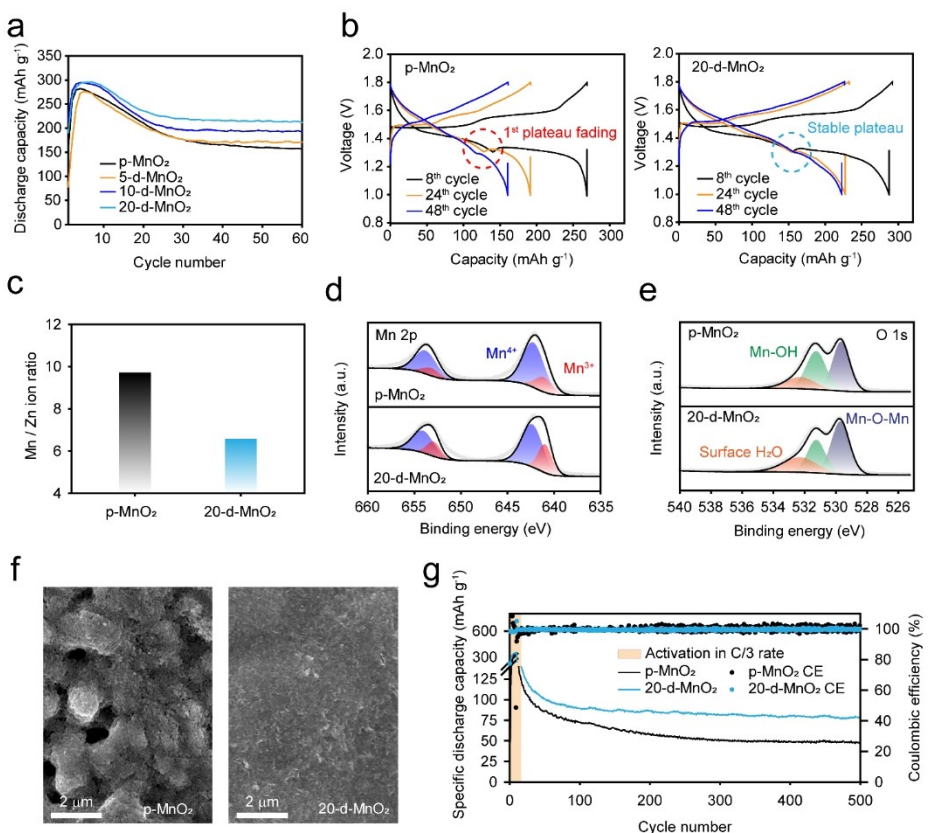


Figure 3. Electrochemical performance of DCDA-coated MnO₂. a) Capacity retention test at C/3 rate for zinc ion batteries with p-, 5-d-, 10-d-, and 20-d-MnO₂. b) Charge and discharge voltage profiles for p-MnO₂ and 20-d-MnO₂ at selected cycles. c-f) Post-mortem analysis of p-MnO₂ and 20-d-MnO₂ after the 30th discharge step of C/3 rate cycling. d) ICP analysis of the electrolytes taken from the cells, e) Mn 2p and f) O 1s XPS spectra, and g) SEM image of the p-MnO₂ and 20-d-MnO₂ cathodes after cycling. g) Comparison of 1C rate cycling performance between p-MnO₂ and 20-d-MnO₂ cathode.

uted to Mn—O—Mn and Mn—OH bonds at 529.7 and 531.3 eV, respectively [Figure 3(e)].^[40,41] In agreement with the Mn XPS and ICP analysis, the relative intensity was lower for the 20-d-MnO₂ electrode (0.56) than that for p-MnO₂ (0.90), verifying the lower degree of Mn dissolution for 20-d-MnO₂.

The SEM images of the p-MnO₂ and 20-d-MnO₂ electrodes after the cell test show stark differences in morphology [Figure 3(f)]. For p-MnO₂, a rough pitted surface was observed, indicating the occurrence of significant Mn dissolution. However, the smooth and uniform surface of 20-d-MnO₂ cathode suggests attenuated Mn dissolution. A comparison of the XRD patterns of the discharged cathodes after the cycling test further indicates the higher stability of 20-d-MnO₂ (Figure S3). The peaks from zinc manganese oxide were more pronounced for 20-d-MnO₂, indicating that the structure was preserved to a larger degree during the cycling test.

To further reveal the different degradation behavior of the 1st plateau observed in the low C-rate condition test, high C-rate (1C rate) operation was conducted in the voltage range of 1.3–1.8 V. The lower cut-off voltage (1.3 V) was selected to exclude the irreversible Zn²⁺ intercalation/de-intercalation reaction. C/3 rate cycling with the conventional voltage range (1–1.8 V) of MnO₂ was pre-cycled before the high C-rate condition in order to activate the MnO₂. As seen in Figure 3(g),

the 20-d-MnO₂ electrode showed about 170% higher capacity at 500 cycles compared with p-MnO₂ and an average coulombic efficiency (CE) of 99.9% whereas p-MnO₂ showed fluctuating CE with a low value (99.2%). The voltage profiles of the 100th, 200th, and 300th cycles of each cell again confirm the efficacy of DCDA coating; the 20-d-MnO₂ electrode showed stable profile in contrast to the severe degradation of the p-MnO₂ electrode (Figure S4). Such difference in discharge capacity retention between p-MnO₂ and 20-d-MnO₂ was also found in conventional voltage range (1–1.8 V) with MnSO₄-containing 2M ZnSO₄ electrolyte at 1C rate or with MnSO₄-free 2M ZnSO₄ electrolyte at C/3 rate as shown in Figure S5, demonstrating the generality of the effect of DCDA coating. However, it should be mentioned that there are some increase of interfacial resistance as it is shown in Figure S6.

2.3. Alleviated Lattice Distortion with the DCDA Coating

To verify the DCDA-induced structural changes in MnO₂, the XRD patterns of p-, 5-d-, 10-d-, and 20-d-MnO₂ powder samples were compared. In here, silicon powders were added to the samples as an internal reference to accurately scrutinize the shift of XRD peaks (resolution limit ~0.001 degree). The XRD

spectra, which are aligned with respect to the peak from Si powder at 28° , are compared in Figure 4(a). Interestingly, the [001] peak shifted to higher 2θ with increased DCDA content, indicating the reduction of the interlayer distance. The change in the crystallographic structure is supported by the Raman spectroscopy analysis results [Figure 4(b)]. The Raman signals of δ -MnO₂ feature two representative bands:^[42,43] in-plane vibration of the Mn–O bond at 575 cm^{-1} and out-of-plane vibration of the Mn–O bond perpendicular to the layers at 630 cm^{-1} . Two bands were detected for the p-, 5-d-, 10-d-, and 20-d-MnO₂ electrodes. The in-plane vibration peak, which is insensitive to lattice distance, did not vary with the DCDA content. However, the out-of-plane vibration band was shifted to a lower wavenumber (red-shift) with the DCDA content, indicating elongation of Mn–O bond perpendicular to the layer and the contraction of the MnO₂ layers with the DCDA coating, as was observed by XRD analysis.^[44]

Figure 4(c) shows the UV photoelectron spectroscopy (UPS) result of p-MnO₂ and 20-d-MnO₂. The binding energy at the onset of the band was higher for 20-d-MnO₂ by 0.4 eV, implying that the energy state of the O_{2p} orbital in the MnO₂ layer was lowered by DCDA. It should be mentioned that the energy state related with Mn³⁺ was located at a lower binding energy; however, it could not be observed because of limited resolution. It was previously reported that the steric strain due to the difference in crystal structure between Jahn-Teller (JT)-active Mn³⁺ and JT-inactive Mn⁴⁺ in MnO₂ slab can elevate the O_{2p} energy level.^[42] In that sense, the relaxation of oxygen species indicates that the DCDA coating minimized the MnO₂ lattice structure differences between [MnO₆]³⁺ and [MnO₆]⁴⁺, resulting in a highly-uniform lattice and alleviated steric strain in the MnO₂ slab. Because the decreased lattice distance also

indicates a reduced buckling and better uniformity of MnO₂ lattice as the lattice mismatch can increase the interlayer spacing,^[45] these analyses collectively support that the uniform MnO₂ lattice without any buckling can be obtained by virtue of the DCDA treatment.

High-resolution transmission electron microscopy (HRTEM) analysis was further carried out to show DCDA coating improves the lattice uniformity. As seen in Figure 4d, p-MnO₂ exhibited a distorted and fragmented uneven lattice structure like other δ -MnO₂ lattice morphologies previously reported.^[13,36,46] By sharp contrast, 20-d-MnO₂ showed a highly-oriented lattice structure without any distortion or defects, clearly demonstrating that the δ -MnO₂ lattice distortion was alleviated with DCDA. Moreover, the lattice distance identified in the TEM images was shorter for 20-d-MnO₂ by 0.1 Å, which is in good agreement with the XRD and Raman analysis results. It should be also mentioned that lattice uniformity difference between p-MnO₂ and 20-d-MnO₂ was clearly shown even after 30 cycles (Figure S7). It verifies that the structural change induced by DCDA is maintained during cycling.

2.4. DCDA-Driven Cooperative Jahn-Teller Distortion around Mn⁴⁺

To study the molecular mechanism behind the DCDA-driven structural changes in the δ -MnO₂ lattice and improved MnO₂ stability, density functional theory (DFT) calculations were performed. For the analysis, two model MnO₂ systems were constructed; one describes the system prior to DCDA adsorption and the other after DCDA adsorption. The DCDA-adsorbed systems were constructed after DFT optimization of the pristine

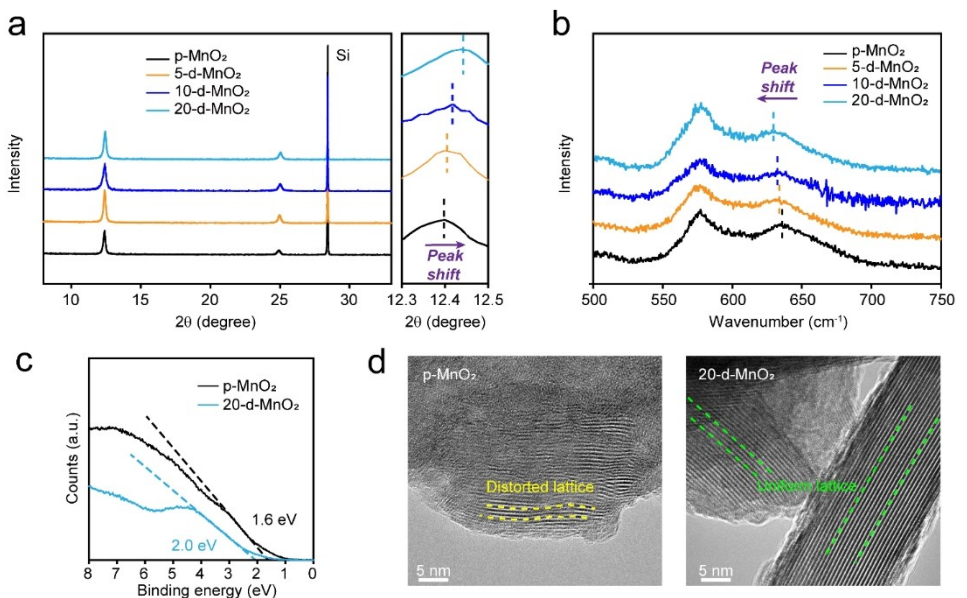


Figure 4. Change in δ -MnO₂ structure with the DCDA coating. Comparison of a) XRD patterns for p-, 5-d-, 10-d-, and 20-d-MnO₂ electrodes containing Si powder as an internal reference and of b) Raman spectra for p-, 5-d-, 10-d-, and 20-d-MnO₂ electrodes. c) UPS spectra and d) high-resolution TEM images of p-MnO₂ and 20-d-MnO₂ electrodes.

system. For the DCDA-coated MnO_2 system, DCDA was found to adsorb to the surface of MnO_2 with its amine groups and participate in strong donor-acceptor interactions with the surface oxygen atoms. Given the abundance of potential adsorption sites, several adsorption scenarios were considered. The structures of the resulting systems are shown in Figures S8–S15.

The projected density of states (PDOS) of MnO_2 before and after DCDA treatment were then calculated, and the results are presented in Figure 5(a). Interestingly, significant differences in the electronic structures of the two systems were observed. First of all, notable lowering of the lowest unoccupied molecular orbital (LUMO) of Mn^{4+} affected by DCDA was observed, which strongly indicates that CJTD had taken place for this Mn^{4+} species. This effect was further confirmed by the band-decomposed charge density plot of the said LUMO shown in Figure 5(b). The charge density was found to be localized around the Mn^{4+} affected by DCDA, confirming that CJTD had taken place for this Mn^{4+} ; hence, the newly observed peak is primarily assigned to the said species. Secondly, the highest occupied molecular orbital (HOMO) of Mn^{3+} shifted to a lower energy level, which suggests that the Mn^{3+} closest to the adsorbed DCDA underwent further JTD. Along with the lowering of Mn^{3+} , shift in fermi level was also observed in both PDOS and the work function analysis (Figure S16). This results clearly demonstrate further relaxation of Mn^{3+} via surrounding CJTD of Mn^{4+} . Finally, the energy states of O_{2p} were also observed at a lower position, which is consistent with the UPS result and altogether implies improved lattice uniformity due to the CJTD. To further validate our computational results, the band gaps of p- MnO_2 and 20-d- MnO_2 were experimentally determined from their reflection electron energy loss spectra (REELS). As presented in Figure S17, DCDA treatment led to a decrease in the band gap due to the lowering of LUMO, which corroborates the findings from the PDOS calculations. PDOS analysis was also performed for the other DCDA adsorption scenarios, and a consistent set of changes in the electronic structures was successfully observed (Figure S18).

The local geometries of the $[\text{MnO}_6]^{4+}$ octahedral complex before and after DCDA adsorption are presented in Figure 5(c). Interestingly, the Mn–O bond underwent notable elongation after DCDA treatment along a single axis of the octahedral complex. Such structural transformation affirms the occurrence of CJTD around Mn^{4+} as a result of its interaction with DCDA.^[47] Due to the limited system size and calculation constraints used in the DFT calculations, however, overall improvement in lattice uniformity arising from CJTD-induced structural changes could not be directly observed. Nevertheless, it is conjectured that the geometric and energetic changes of the system with the onset of CJTD triggered by DCDA would also lead to the stabilization of nearby Mn^{3+} . As such, the steric stress arising from the coexistence of Mn^{3+} and Mn^{4+} is reduced, improving the overall lattice uniformity.

The DFT results also present evidence of the π donor-acceptor interaction between DCDA and $[\text{MnO}_6]$ complex. The charge density difference (CDD) plot with DCDA adsorption is displayed in Figure S19. The plot shows that the charge density of the surface oxygen atoms significantly increased with the adsorption of DCDA, verifying strong donor-acceptor interactions.^[30] Due to the varied charge densities, the octahedral structure of the $[\text{MnO}_6]^{4+}$ rearranges into an elongated configuration. Traditionally, serious JTD in intercalating cathodes is acknowledged to be disadvantageous for battery performance. However, recent reports show that exercising control over such Jahn-Teller effects can improve cathode stability and performance for the intercalation process.^[48,49] Because CD reaction is the main cause of battery failure in mildly acidic conditions, we believe triggering CJTD for Mn^{4+} and further promoting the JTD of Mn^{3+} by surface coating of MnO_2 with DCDA can result in notable improvement in the cycling performance of MnO_2 .

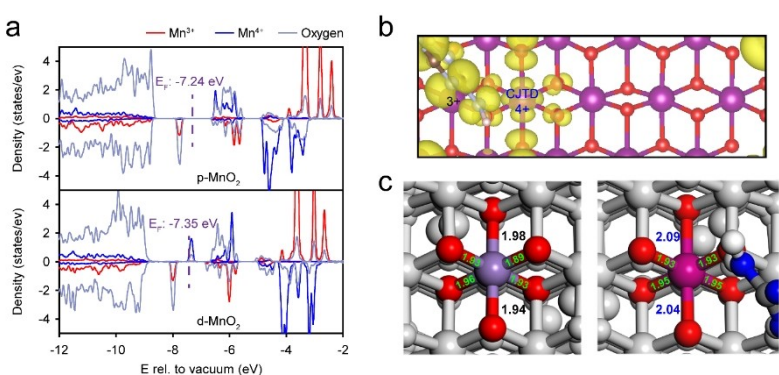


Figure 5. Electronic structure analyses of p- MnO_2 and d- MnO_2 . a) Projected density of states (PDOS) plots for p- MnO_2 (top) and d- MnO_2 (bottom). b) Band-decomposed charge density plot of the conduction band minimum (CBM) in d- MnO_2 . Plot is drawn for the uppermost layer of the MnO_2 model system where DCDA has been adsorbed. Nonzero charge densities are found exclusively around the CJTD-induced Mn^{4+} and DCDA. c) Local geometry of the $[\text{MnO}_6]^{4+}$ complex before (left) and after (right) CJTD with DCDA adsorption. Mn–O bond lengths are reported in Angstroms. Bond length values for the elongated z-axis are shown in black (left) and blue (right).

3. Conclusions

In this work, we have demonstrated that coating the surface of MnO_2 with DCDA can improve the stability of MnO_2 in ZIBs by triggering cooperative Jahn-Teller distortion of Mn^{4+} and further promoting Jahn-Teller distortion of Mn^{3+} . Such Jahn-Teller distortion reactions serve as alternative ways of resolving the orbital degeneracy of Mn^{3+} without undergoing charge disproportionation of Mn^{3+} and subsequent Mn dissolution. With the proposed DCDA treatment, significant reduction of Mn dissolution was observed, which resulted in ~170% higher capacity in comparison with pristine MnO_2 . Improved cell performance was attributed to the higher lattice uniformity that was consistently observed in XRD, Raman, UPS, and TEM analyses. From the DFT calculations, it was found that CJTD takes place in the DCDA-coated MnO_2 from the interactions between DCDA and $[\text{MnO}_6]^{4+}$, which was effectively confirmed by the changes in the energy states of MnO_2 and the geometry of the affected $[\text{MnO}_6]$ complex. Based on these results, we postulate that CJTD would release the internal stress between inner-lattice species while also stabilizing Mn^{3+} by resolving orbital degeneracy, consequently preventing the charge disproportionation reaction from taking place. We believe our findings will provide a new pathway toward developing high-performance Zn ion batteries with MnO_2 cathodes.

Experimental Section

Material preparation

The $\delta\text{-MnO}_2$ particles were prepared by a thermal decomposition method used in previous studies.^[18] For the typical conditions, KMnO_4 powder was heated at 500 °C (heating rate of 5 °C/min) for 5 h using a tube furnace and rested to cool naturally until it reached room temperature. The obtained powder was then washed thoroughly with DI water 6 times by centrifugation and dried at 60 °C for more than 12 h under vacuum. The as-prepared MnO_2 was coated with DCDA by using the wet coating method. Specifically, the required amounts of MnO_2 and DCDA were dispersed in DI water by using a bath sonicator to uniformly coat DCDA onto the surface of MnO_2 . The dispersed solution was kept under stirring for more than 48 h at 70 °C, and then the DCDA-coated MnO_2 was collected in powder form.

Characterization

The morphology of the samples was imaged by scanning electron microscopy (SEM; Sirion, FEI), and transmission electron microscopy (TEM; Talos F200X, Tecnai G² F30 S-TWIN, FEI). The distribution of elements in each sample was characterized by scanning TEM energy dispersive spectroscopy (STEM-EDS; FEI). The chemical states of MnO_2 powders were investigated by X-ray photoelectron spectroscopy (XPS; Al K-alpha, Thermo VG Scientific) analysis. Crystalline information was collected by X-ray diffractometry (XRD; Smartlab, RIGAKU), and Raman spectroscopy (LabRam HR Evolution Visible_NIR, HORIBA). The dissolution of Mn ions into the electrolytes during the cell test was quantified by inductively coupled plasma atomic emission spectroscopy (ICP-OES; OPTIMA 7300 DV). The electronic structure of the samples was analyzed by using ultraviolet photoelectron spectroscopy (UPS; Axis-supra, Kratos)

and reflection electron energy loss spectra (REELS; Axis-supra, Kratos).

Electrochemical performance

Electrochemical tests were conducted using CR2032 coin-type cells. The coin cells were composed of a working electrode (MnO_2 cathode), a glass fiber separator, zinc metal as a counter electrode, and the electrolyte (2 M ZnSO_4 with 0.2 M MnSO_4). To fabricate a working electrode, MnO_2 slurry was prepared by mixing the active material (MnO_2), conductive material (Super P carbon), and binder (polyvinylidene fluoride; PVdF) at a weight ratio of 7:2:1 with an appropriate amount of 1-dimethyl-2-pyrrolidone (NMP) as a solvent. Hydrophilic carbon paper was selected as the current collector for the working electrode, and as-prepared MnO_2 slurry was coated on the carbon paper by using a doctor blade. The areal loading of MnO_2 was maintained in the range of 2 to 4 mg cm^{-2} . Galvanostatic charge-discharge (GCD) tests of the assembled cells were conducted in the voltage range of 1 to 1.8 V using the TOSCAT-3000U (Toyo System). For the electrochemical impedance spectroscopy (EIS) test, the BioLogic VSP electrochemical workstation was used. The EIS was measured in the frequency range from 0.01 to 10^5 Hz with the coin-type assembled cells.

Computational methods

All DFT calculations were performed with the Vienna *Ab initio* Simulation Package (VASP) version 5.4.4. The projector augmented wave (PAW) method with Perdew-Burke-Ernzerhof exchange-correlation functional was used.^[50,51] Spin polarization was considered in all calculations. For an accurate consideration of the on-site coulombic interactions, the U correction method was used, where the U_{eff} value of 5.0 was used for the Mn ions.^[52] The energy cutoff was set to be 520 eV, and k-point spacing of 0.3 Å⁻¹ was used with the Monkhorst-Pack scheme. The energy convergence criterion was set at 1×10^{-6} eV, and geometry optimization was performed until the maximum atomic force for each atom became lower than 0.01 eV/Å.

Model MnO_2 systems were constructed by starting from a 5×2 supercell of bulk, hexagonal MnO_2 . After the relaxation of the bulk supercell, a slab model of was constructed by further expanding the system in the z-axial direction to create three MnO_2 layers, then also introducing a 20 Å vacuum layer along the same direction. Here, 8 K^+ cations were also intercalated into the two interstices of the MnO_2 layers, effectively creating a $\text{K}_{0.26}\text{MnO}_2$ model system that closely matched the experimentally observed $\text{K}_{0.25}\text{MnO}_2$. The oxidation states of Mn ions were determined by examining the magnetic moments of each Mn ion in the calculation results. Energy alignment to vacuum was performed by using Macro-Density software.

Acknowledgements

This research was supported by the '2021 Joint Research Project of Institutes of Science and Technology', and the National Research Foundation of Korea (NRF) funded by the Ministry of Science and ICT (NRF-2020M3H4A1A03082979).

Conflict of Interest

The authors declare no conflict of interest.

Keywords: charge disproportionation · Jahn-Teller distortion · Manganese oxide · Orbital degeneracy · Zinc ion batteries

- [1] L. Ma, M. A. Schroeder, O. Borodin, T. P. Pollard, M. S. Ding, C. Wang, K. Xu, *Nat. Energy* **2020**, *5*, 743–749.
- [2] Y. Jin, L. Zou, L. Liu, M. H. Engelhard, R. L. Patel, Z. Nie, K. S. Han, Y. Shao, C. Wang, J. Zhu, H. Pan, J. Liu, *Adv. Mater.* **2019**, *31*, 1900567.
- [3] Z. Zhao, J. Zhao, Z. Hu, J. Li, J. Li, Y. Zhang, C. Wang, G. Cui, *Energy Environ. Sci.* **2019**, *12*, 1938–1949.
- [4] J. Gao, X. Xie, S. Liang, B. Lu, J. Zhou, *Nano-Micro Lett.* **2021**, *13*, 69.
- [5] L. Cao, D. Li, T. Deng, Q. Li, C. Wang, *Angew. Chem. Int. Ed.* **2020**, *59*, 19292–19296; *Angew. Chem.* **2020**, *132*, 19454–19458.
- [6] Y. Zhao, Y. Zhu, X. Zhang, *InfoMat* **2020**, *2*, 237–260.
- [7] J. Hao, X. Li, S. Zhang, F. Yang, X. Zeng, S. Zhang, G. Bo, C. Wang, Z. Guo, *Adv. Funct. Mater.* **2020**, *30*, 2001263.
- [8] L. Ma, S. Chen, C. Long, X. Li, Y. Zhao, Z. Liu, Z. Huang, B. Dong, J. A. Zapien, C. Zhi, *Adv. Energy Mater.* **2019**, *9*, 1902446.
- [9] D. Kundu, B. D. Adams, V. Duffort, S. H. Vajargah, L. F. Nazar, *Nat. Energy* **2016**, *1*, 16119.
- [10] C. Kim, B. Y. Ahn, T.-S. Wei, Y. Jo, S. Jeong, Y. Choi, I.-D. Kim, J. A. Lewis, *ACS Nano* **2018**, *12*, 11838–11846.
- [11] L. Zhang, L. Chen, X. Zhou, Z. Liu, *Adv. Energy Mater.* **2015**, *5*, 1400930.
- [12] L. Shan, Y. Wang, S. Liang, B. Tang, Y. Yang, Z. Wang, B. Lu, J. Zhou, *InfoMat* **2021**, inf2.12223.
- [13] Y. Jiang, D. Ba, Y. Li, J. Liu, *Adv. Sci.* **2020**, *7*, 1902795.
- [14] C. Guo, H. Liu, J. Li, Z. Hou, J. Liang, J. Zhou, Y. Zhu, Y. Qian, *Electrochim. Acta* **2019**, *304*, 370–377.
- [15] J. Yan, Z. Fan, T. Wei, W. Qian, M. Zhang, F. Wei, *Carbon* **2010**, *48*, 3825–3833.
- [16] D. Gueon, J. H. Moon, *ACS Sustainable Chem. Eng.* **2017**, *5*, 2445–2453.
- [17] H. Pan, Y. Shao, P. Yan, Y. Cheng, K. S. Han, Z. Nie, C. Wang, J. Yang, X. Li, P. Bhattacharya, K. T. Mueller, J. Liu, *Nat. Energy* **2016**, *1*, 16039.
- [18] M. H. Alfaruqi, S. Islam, D. Y. Putro, V. Mathew, S. Kim, J. Jo, S. Kim, Y.-K. Sun, K. Kim, J. Kim, *Electrochim. Acta* **2018**, *276*, 1–11.
- [19] Y. Fu, Q. Wei, G. Zhang, X. Wang, J. Zhang, Y. Hu, D. Wang, L. Zuin, T. Zhou, Y. Wu, S. Sun, *Adv. Energy Mater.* **2018**, *8*, 1801445.
- [20] Y. Liu, J. Zhi, M. Sedighi, M. Han, Q. Shi, Y. Wu, P. Chen, *Adv. Energy Mater.* **2020**, *10*, 2002578.
- [21] Z. Hou, M. Dong, Y. Xiong, X. Zhang, H. Ao, M. Liu, Y. Zhu, Y. Qian, *Small* **2020**, *16*, 2001228.
- [22] J. Huang, Z. Wang, M. Hou, X. Dong, Y. Liu, Y. Wang, Y. Xia, *Nat. Commun.* **2018**, *9*, 2906.
- [23] K. W. Nam, H. Kim, J. H. Choi, J. W. Choi, *Energy Environ. Sci.* **2019**, *12*, 1999–2009.
- [24] W.-W. Liu, D. Wang, Z. Wang, J. Deng, W.-M. Lau, Y. Zhang, *Phys. Chem. Chem. Phys.* **2017**, *19*, 6481–6486.
- [25] C. A. Marianetti, D. Morgan, G. Ceder, *Phys. Rev. B* **2001**, *63*, 224304.
- [26] A. M. Stoneham, M. Lannoo, *J. Phys. Chem. Solids* **1969**, *30*, 1769–1777.
- [27] F. F. Marafatto, M. L. Strader, J. Gonzalez-Holguera, A. Schwartzberg, B. Gilbert, J. Peña, *Proc. Nat. Acad. Sci.* **2015**, *112*, 4600–4605.
- [28] A. Chakravarty, D. Sengupta, B. Basu, A. Mukherjee, G. De, *RSC Adv.* **2015**, *5*, 92585–92595.
- [29] B. K. Sharma, A. M. Shaikh, N. Agarwal, R. M. Kamble, *RSC Adv.* **2016**, *6*, 17129–17137.
- [30] F. A. Armstrong, *Phil. Trans. R. Soc. B* **2008**, *363*, 1263–1270.
- [31] T. Takashima, K. Hashimoto, R. Nakamura, *J. Am. Chem. Soc.* **2012**, *134*, 18153–18156.
- [32] K. Chen, M. Wang, G. Li, Q. He, J. Liu, F. Li, *Materials* **2018**, *11*, 601.
- [33] G. Li, Z. Huang, J. Chen, F. Yao, J. Liu, O. L. Li, S. Sun, Z. Shi, *J. Mater. Chem. A* **2020**, *8*, 1975–1985.
- [34] X. Zeng, J. Liu, J. Mao, J. Hao, Z. Wang, S. Zhou, C. D. Ling, Z. Guo, *Adv. Energy Mater.* **2020**, *10*, 1904163.
- [35] J. Long, F. Yang, J. Cuan, J. Wu, Z. Yang, H. Jiang, R. Song, W. Song, J. Mao, Z. Guo, *ACS Appl. Mater. Interfaces* **2020**, *12*, 32526–32535.
- [36] T. Sun, Q. Nian, S. Zheng, J. Shi, Z. Tao, *Small* **2020**, *16*, e2000597.
- [37] C. Wu, H. Tan, W. Huang, W. Li, K. N. Dinh, C. Yan, W. Wei, L. Chen, Q. Yan, *Adv. Funct. Mater.* **2020**, *30*, 2003187.
- [38] W. Sun, F. Wang, S. Hou, C. Yang, X. Fan, Z. Ma, T. Gao, F. Han, R. Hu, M. Zhu, C. Wang, *J. Am. Chem. Soc.* **2017**, *139*, 9775–9778.
- [39] D. Wang, L. Wang, G. Liang, H. Li, Z. Liu, Z. Tang, J. Liang, C. Zhi, *ACS Nano* **2019**, *13*, 10643–10652.
- [40] G. Xie, X. Liu, Q. Li, H. Lin, Y. Li, M. Nie, L. Qin, *J. Mater. Sci.* **2017**, *52*, 10915–10926.
- [41] Y. Wu, J. Fee, Z. Tobin, A. Shirazi-Amin, P. Kerns, S. Dissanayake, A. Mirich, S. L. Suib, *ACS Appl. Mater. Interfaces* **2020**, *3*, 1627–1633.
- [42] Z. Morgan Chan, D. A. Kitchev, J. Nelson Weker, C. Schnedermann, K. Lim, G. Ceder, W. Tumas, M. F. Toney, D. G. Nocera, *Proc. Nat. Acad. Sci.* **2018**, *115*, E5261–E5268.
- [43] C. Zhu, L. Yang, J. K. Seo, X. Zhang, S. Wang, J. Shin, D. Chao, H. Zhang, Y. S. Meng, H. J. Fan, *Mater. Horiz.* **2017**, *4*, 415–422.
- [44] C. Julien, *Solid State Ionics* **2003**, *159*, 345–356.
- [45] Q. Chu, X. Wang, X. Zhang, Q. Li, X. Liu, *Inorg. Chem.* **2011**, *50*, 2049–2051.
- [46] C. Qiu, X. Zhu, L. Xue, M. Ni, Y. Zhao, B. Liu, H. Xia, *Electrochim. Acta* **2020**, *351*, 136445.
- [47] G. A. Gehring, K. A. Gehring, *Rep. Prog. Phys.* **1975**, *38*, 1–89.
- [48] H. Chen, C. L. Freeman, J. H. Harding, *Phys. Rev. B* **2011**, *84*, 085108.
- [49] P.-F. Wang, T. Jin, J. Zhang, Q.-C. Wang, X. Ji, C. Cui, N. Piao, S. Liu, J. Xu, X.-Q. Yang, C. Wang, *Nano Energy* **2020**, *77*, 105167.
- [50] P. E. Blöchl, *Phys. Rev. B* **1994**, *50*, 17953–17979.
- [51] J. P. Perdew, K. Burke, M. Ernzerhof, *Phys. Rev. Lett.* **1996**, *77*, 3865–3868.
- [52] E. de la Llave, E. Talaie, E. Levi, P. K. Nayak, M. Dixit, P. T. Rao, P. Hartmann, F. Chesneau, D. T. Major, M. Greenstein, D. Aurbach, L. F. Nazar, *Chem. Mater.* **2016**, *28*, 9064–9076.

Manuscript received: July 26, 2021

Revised manuscript received: August 30, 2021

Accepted manuscript online: September 8, 2021

Version of record online: September 29, 2021